

Mapping Encoder Values to Ankle Angles in a 3 DoF Parallel Ankle Exoskeleton

Miha Dežman^{*†}, Charlotte Marquardt^{*} and Tamim Asfour^{*†}

Abstract—Accurate estimation of ankle joint angles is vital for advancing assistive technologies such as ankle exoskeletons. This study investigates whether three encoders within the parallel kinematics of a three degree of freedom (3-DoF) ankle exoskeleton can effectively estimate the three rotational movements of the ankle: plantar-/dorsiflexion (PF/DF), in-/eversion (IN/EV), and internal/external rotation (IR/ER). Performance was tested during walking, curve walking, and stair climbing with two healthy participants. Ankle motion was independently captured using a motion capture system, while encoder values from the exoskeleton were concurrently recorded. The root-mean-squared error (RMSE) for angle estimations ranged from 1° and 3°, indicating good accuracy, particularly for IN/EV and IR/ER, though challenges were noted in capturing peak dorsiflexion. The findings suggest that misalignment between the exoskeleton and the biological joint axis may have contributed to the observed inaccuracies, particularly for PF/DF, as evidenced by differing range of motion (RoM). Additionally, variability between the two participants may reflect the potential impact of individual anthropometry and alignment quality, which could inform future considerations for design and alignment protocols. Future model enhancements could incorporate dynamic effects and machine learning to generalize across diverse populations.

I. INTRODUCTION

Exoskeletons have emerged as innovative assistive devices designed to enhance mobility, support rehabilitation, and improve the overall quality of life for individuals with various physical impairments. Among these, ankle exoskeletons specifically target the ankle joint, providing assistance to reduce the metabolic cost of walking. These systems enable users to regain or enhance movement patterns that may have been disrupted due to injury or disease [1], [2].

A critical aspect of optimizing ankle exoskeletons is the accurate estimation of ankle joint kinematics, which is essential for delivering customized assistance across the three degree of freedom (DoF) of the ankle: plantar-/dorsiflexion (PF/DF), in-/eversion (IN/EV), and internal/external rotation (IR/ER). However, determining the precise motion of the ankle joint is inherently complex due to the necessity of three-dimensional imaging techniques, which are vital for capturing the intricate movements of the ankle [3]–[5]. These imaging techniques provide valuable data but can be resource-intensive and not always accessible in all clinical or research settings.

This work has been supported by the Carl Zeiss Foundation through the JuBot project and the German Federal Ministry of Education and Research (BMBF) under the Robotics Institute Germany (RIG).

^{*}High Performance Humanoid Technologies Lab, Institute for Anthropomatics and Robotics, Karlsruhe Institute of Technology (KIT), Germany

[†]Corresponding authors: {miha.dezman, asfour}@kit.edu

The integration of sensors into exoskeletons marks an advancement in the continuous monitoring and analysis of user data, particularly concerning motor performance [6]. These devices can provide real-time feedback, enhancing the understanding of joint kinematics and thereby improving rehabilitation protocols and performance assessments. However, most wearable exoskeleton designs primarily optimize for PF/DF motion, offering limited motion or assistance for IN/EV and IR/ER [7], [8]. A notable example is the wearable three DoF exoskeleton developed by Weerasingha et al. [9], which incorporates direct angle measurement via encoders and allows for assistance. However, this system is constrained by its considerable weight and limited torque assistance, highlighting the ongoing challenge of balancing functionality and portability in exoskeleton design. Another three DoF ankle exoskeleton mechanism by Hong et al. [10] uses a configuration of three encoders integrated into a spherical mechanism. These measure all rotations of the ankle joint. However, the proposed device does not include a method for actuation and active assistance. Lack of a rigid supportive three DoF structure requires multi-DoF measurement methods or external sensing systems to determine the accurate state of the exoskeleton. Such an example is the three DoF exoskeleton by Mooney et al. [11], which utilizes struts attached to a hiking boot for torque transmission, facilitating some IN/EV and IR/ER movements. Struts deformations were measured using motion capture (MOCAP) to estimate assistance torques, allowing for a simplified exoskeleton design but limiting its use to a laboratory setting.

Multidimensional DoF measurement of the ankle is also possible with systems exploiting magnetic fields for actuation and sensing [12]. However, the findings indicate that while magnetic fields can facilitate complex motion tracking, they require specialized calibration setups to ensure accuracy, showing the complexities involved in kinematic measurement within multi-DoF systems.

Soft exosuits allow minimally restrictive motion of user joints with structures relying on fabric materials and cables for force transmission. These exoskeletons represent a lightweight alternative with excellent adaptability to various postures and dynamic movements [13], [14]. However, their inherent compliance introduces challenges in achieving accurate kinematic assessments. This difficulty arises primarily from the non-rigid nature of their components and the lack of rigid attachment points, which complicates the use of conventional angular encoder measurements. Instead, novel sensor systems and technologies are proposed, including optoelectronic systems [15], stretchable sensors [16], and

capacitance-based bending sensors [17], to facilitate continuous monitoring of joint angles. To address these challenges, novel sensor systems and technologies have been proposed, including optoelectronic systems [15], stretchable sensors [16], and capacitance-based bending sensors [17], to facilitate continuous monitoring of joint angles despite the adaptability of exosuits. However, these novel sensors are not yet widely accessible.

Alternatively, inertial measurement unit (IMU) sensors are frequently employed for tracking motion in wearable devices, which includes both rigid and soft exoskeletons. Chapman et al. [18] validated IMU-based methods against optical MOCAP systems, demonstrating high accuracy for upper extremity movements. Similarly, Kim et al. [19] confirmed the reliability of IMU sensors in tracking ankle kinematics during running. The quality of measurements can be enhanced through sensor fusion techniques that integrate different modalities. For example, Arceo et al. [20] developed a robust system that combines force sensing resistor (FSR) and IMU sensors to measure both force myography (FMG) signals and limb motion. However, while IMU sensors offer practical solutions for motion tracking, they require extensive calibration to ensure accuracy, and there may be inherent limitations to the precision they can achieve due to factors such as drift and sensor misalignment [21], [22].

This study builds upon prior work to evaluate the feasibility of a 3-DoF ankle exoskeleton equipped with encoders for joint angle estimation [7]. The kinematic design of the ankle exoskeleton enables passive adaptation to IN/EV and IR/ER motion and assistance along PF/DF motion. It features a size adjustable frame and embedded encoders for angle measurement. Notably, the encoders are arranged in a parallel kinematics configuration, meaning that they do not directly represent the three rotations of the ankle joint. This study presents a simplified model to estimate the three ankle rotations based on the encoder values and their combinations. By testing the exoskeleton on two participants during walking, curve walking, and stair-climbing tasks, we examine the system’s ability to capture 3-DoF ankle rotations and assess factors influencing its performance. The findings provide valuable insights into design and alignment improvements necessary for future iterations.

The remainder of this paper is structured as follows. Section II details the design of the exoskeleton device, the user study protocol, and the procedures for data collection, postprocessing, and optimization. Section III presents the experimental results, including an analysis of the system’s performance in estimating 3-DoF ankle rotations. Section IV explores the implications of these findings, highlighting design considerations and future directions for improvement. Finally, Section V summarizes the contributions of this study and outlines potential avenues for further research.

II. METHODS

A. Exoskeleton

This paper builds on the exoskeleton presented in [7]. The exoskeleton consists of a rigid frame structure that includes

a *shank* and a *foot* section, shown in Fig. 1 (left). A series of joints, including a parallelogram mechanism, link the two sections. The *shank* frame has a kinematic design that adjusts to the user’s ankle movements. It incorporates 11 DoF, comprising multiple passive 1 DoF joints as well as two passive 3 DoF joints, as illustrated in Fig. 1(right). Additional

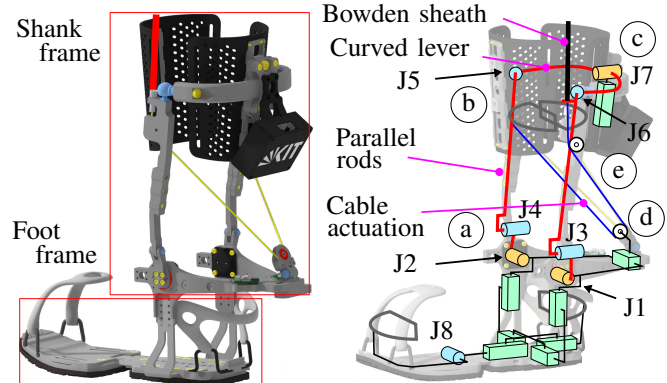
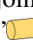
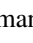

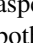


Fig. 1: Exoskeleton shown *left* and the kinematic representation shown *right*. The structure consists of several passive joints: “” 1 rotation DoF joint, “” 3 DoF ball joint, “” 1 rotation DoF with an encoder and “” 1 DoF manually adjustable translation joint. (reused from [7])

aspects of the *shank* frame include: two cylindrical joints on both sides of the exoskeleton (J1, J2, J3, J4) illustrated in Fig. 1 (a), are intentionally misaligned for a more compact integration of the magnetic encoder. The two ball joints (J5, J6) connect each parallel strut to the curved lever, as shown in Fig. 1 (b), allowing for both IN/EV and IR/ER of the ankle. A cylindrical joint (J7) links the curved lever to the exoskeleton cuff, depicted in Fig. 1 (c), and incorporates the third encoder. Altogether, three of the passive joints (J1, J2, J7) include an integrated absolute encoder (RMB20, RLS d.o.o.) to infer the ankle joint angles. The exoskeleton frame is designed to adjust in multiple dimensions for both the *shank* and *foot* frames, as illustrated in Fig. 1(right).

This passive joint configuration permits all three types of ankle rotation, as shown in Fig. 2. When joints J1 and J2 rotate in the same direction, PF/DF movement occurs. The combined rotation of joints J3 and J4 with joints J5 to J7 facilitates the IN/EV motion. Conversely, rotating joints J1 and J2 in opposite directions alongside joints J5 to J7 allows for the IR/ER. An additional foot frame DoF allows for forefoot rotation.

The *foot* frame design is rigid with one passive DoF for rotation of the forefoot, and several adjustable DoF to fit different shoe sizes. The shoe is secured using toe and heel bails adopted from crampons (Petzl, France).

B. User-study

This user study evaluates the proposed encoder model’s effectiveness in estimating the three rotational movements of the ankle across three tasks. Effectiveness is assessed by comparing actual ankle motion, measured independently

TABLE I: Participant Information

Participant	Sex	Height (cm)	Weight (kg)	EU shoe size	Age (y)
pA	female	170	59	40	27
pB	male	178	65	42	22

via MOCAP technology, with ankle measurements from the exoskeleton’s three encoders. Two healthy participants performed activities including straight-path walking, curved-path navigation, and stair ascent and descent. Their demographic and physical details are presented in Table I

Both participants provided written informed consent before the study, which followed the ethical guidelines of the Declaration of Helsinki. The experimental protocol was reviewed and approved by the Karlsruhe Institute of Technology (KIT) Ethics Committee as part of the JuBot project’s ethical application.

The participants engaged in three distinct tasks: 1) *Normal walking*: This task involved walking along a straight path measuring 3 m in length, with two turnarounds that returned them to the starting position. 2) *Figure-eight walking*: In this task, participants maneuvered along a figure-eight path, designed to simulate slalom walking, measuring 3 m in length and 1.5 m in width, starting and ending at the center of the figure-eight. 3) *stair climbing/descending*: Participants ascended a flight of four steps, paused to turn at the top, and then descended back down the stairs before rotating to return to the starting position. These specific tasks were chosen because they represent common and functionally relevant movement patterns in daily activities and exoskeleton applications. The tasks were conducted in a randomized order, with each task repeated three times to ensure consistency in the data collection. Prior to the session, each participant underwent a 3 min familiarization phase, and resting pauses were provided between conditions and repetitions to mini-

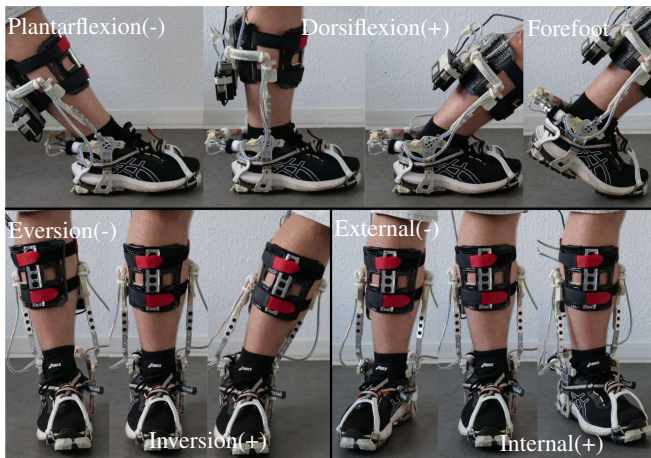


Fig. 2: A display of the exoskeleton’s functionality, highlighting the three main ankle joint rotations: PF/DF, IN/EV, and IR/ER, in addition to the forefoot rotation of the foot frame. (reused from [7])

mize fatigue.

The ankle exoskeleton was fitted to the right leg of each participant and the *foot* frame was adjusted to accommodate the user’s shoe size. During the donning process, the exoskeleton’s PF/DF axis was aligned with the user’s medial malleolus for accurate motion tracking.

The exoskeleton shank was then rotated to achieve symmetry with the sagittal plane and secured in place using adjustable straps. To account for the height of the exoskeleton’s rubber sole, a separate *foot* segment was worn on the left leg, ensuring balanced support during the tasks.

C. Data Collection and Post-Processing

During the experiment, the motion of both the user and the exoskeleton was captured independently across all tasks. Passive markers were placed on the participant to track all three rotational movements of the ankle joint using an optical MOCAP system (Vicon Motion Systems, Ltd., UK). Additionally, the exoskeleton’s internal sensors, including three encoders and a heel switch, were recorded on the exoskeleton side. A combined trigger signal was employed to synchronize the two data sources effectively. The encoders used are RMB14 (RLS d.o.o., Slovenia) that provide a 12-bit resolution. The MOCAP data was sampled at 100 Hz, while the exoskeleton data was collected at 200 Hz.

At the start of each recording, participants were asked to stand in a relaxed position to establish neutral marker positions and neutral positions of the encoders. After the measurements, the MOCAP data was processed to compute the ankle joint angles, as detailed in [7]. The resulting ankle angles calculated with MOCAP are henceforth named as α_{PFDF} , α_{INEV} and α_{IRER} , to denote ankle PF/DF, IN/EV and IR/ER, and present the ground truth for the subsequent analysis. In the same way, the exoskeleton encoder angles are named as ϵ_{LEFT} , ϵ_{RIGHT} and ϵ_{BACK} , representing the encoders at position J1, J2 and J7, respectively, as shown in Fig. 1. To align with the exoskeleton’s sampling frequency, α_{PFDF} , α_{INEV} and α_{IRER} were interpolated to 200 Hz using the *interp1* function in MATLAB®(R2023a, MathWorks, USA).

In all recordings, the mean of the first 100 data points from each of 6 parameters named above was used to calibrate the measurement to the neutral position. For each participant, all recordings related to a specific parameter were concatenated and used to optimize a personalized, user-specific model. To create the generalized model, recordings from all participants were combined. Finally, the distribution of all angles and encoder measurements was calculated using the MATLAB®function *ksdensity*. For visualization, the heel switch measurements marked the beginning of the right stride during straight and figure-eight walking, while MOCAP data was used to identify the start of stair steps.

D. Mathematical Model and Optimization

This section describes the mathematical model and optimization process used for estimation of ankle angles from encoder measurements. For the modeling, a 3D plane equation was used:

$$ax + by + cz = d, \quad (1)$$

where x , y and z represent the three spatial coordinates of the plane, and a , b , c and d are the plane parameters to be determined through optimization.

For easier interpretation and comparison of the plane parameters, Eq. (1) is rearranged into the following form:

$$z = -\frac{a}{c}x - \frac{b}{c}y - \frac{d}{c}. \quad (2)$$

To simplify the notation, we define the terms $-\frac{a}{c}$, $-\frac{b}{c}$, and $-\frac{d}{c}$ as P_1 , P_2 , and P_3 , respectively. This transforms the equation into:

$$z = f_i(x, y) = P_1x + P_2y + P_3, \quad (3)$$

where i is the respective plane fitting. The parameters P_1 , P_2 and P_3 were optimized using the nonlinear programming solver *fmincon* in MATLAB®. An initial guess vector $x_0 = [1, 1, 1]$ was provided, and no bounds were imposed on the search space.

This paper assumes the following parameter relations:

$$\epsilon_{\text{DIFF}} = \epsilon_{\text{LEFT}} - \epsilon_{\text{RIGHT}}, \quad (4)$$

$$\tilde{\alpha}_{\text{PFDF}} = \frac{\epsilon_{\text{LEFT}} + \epsilon_{\text{RIGHT}}}{2} + f_{\text{CPFDF}}(\epsilon_{\text{BACK}}, \epsilon_{\text{DIFF}}), \quad (5)$$

$$\tilde{\alpha}_{\text{INEV}} = f_{\alpha_{\text{INEV}}}(\epsilon_{\text{BACK}}, \epsilon_{\text{DIFF}}), \quad (6)$$

$$\tilde{\alpha}_{\text{IRER}} = f_{\alpha_{\text{IRER}}}(\epsilon_{\text{BACK}}, \epsilon_{\text{DIFF}}), \quad (7)$$

where $f_{\text{CPFDF}}(\epsilon_{\text{BACK}}, \epsilon_{\text{DIFF}})$ is a plane that estimates a correction factor to improve the $\tilde{\alpha}_{\text{PFDF}}$ calculated using the average of ϵ_{LEFT} and ϵ_{RIGHT} . And $\tilde{\alpha}_{\text{INEV}}$ and $\tilde{\alpha}_{\text{IRER}}$ are estimated directly from the corresponding planes $f_{\alpha_{\text{INEV}}}$ and $f_{\alpha_{\text{IRER}}}$, respectively.

III. RESULTS AND ANALYSIS

A. Optimized Parameters

A simple plane fitting was conducted for both individual participants (personalized model) and for the combined data from both participants (generalized model). Table II displays the optimized parameters for the three planes: f_{CPFDF} , $f_{\alpha_{\text{INEV}}}$ and $f_{\alpha_{\text{IRER}}}$, which correspond to the ankle rotations α_{PFDF} , α_{INEV} , and α_{IRER} , respectively. While $f_{\alpha_{\text{INEV}}}$ and $f_{\alpha_{\text{IRER}}}$ directly represent the estimated ankle angles, f_{CPFDF} functions as a correction factor that is added to the average readings

from the left and right encoders. This correction improves the estimation the PF/DF angle, as shown in Eq. (5).

The goodness of fit for each plane is assessed using the RMSE, with lower values indicating a closer alignment to the recorded data. Table II presents the RMSE values calculated for both the individualized models and the generalized model. The table comprises three rows: one for the individual models of participants pA and pB, and another for the generalized model (pAB). The parameters P_1 , P_2 , and P_3 define the orientation of each plane relative to the three axes, providing insight into how well the models represent the actual ankle movements. Normalized RMSE values from this table are presented in Table III to account for different range of motion (RoM).

Participant pB consistently demonstrates the lowest RMSE values across all three parameters (f_{CPFDF} , $f_{\alpha_{\text{INEV}}}$, $f_{\alpha_{\text{IRER}}}$), indicating the most accurate fit of the modeled planes. Notably, the RMSE values for participant pB are smaller for nearly 30% of those recorded for participant pA in both f_{CPFDF} and $f_{\alpha_{\text{INEV}}}$. This disparity suggests that participant pB's movement patterns align more closely with the modeled planes, resulting in a superior fit. In contrast, participant pA exhibits higher RMSE values for all parameters, underscoring a less precise correspondence between their motion and the fitted model.

The generalized model (pAB) yields root RMSE values that lie between those of the individual participants. This suggests that while the combined model captures overarching trends across both participants, it sacrifices some specificity achieved by the individualized models. Although the generalized model results in slightly higher RMSE values, the differences are relatively small, indicating that it could serve as a practical approximation. Nonetheless, its performance may still be enhanced through further fine-tuning for each participant to improve accuracy.

The plane parameters P_1 , P_2 , and P_3 provide valuable insights into the relative contributions of the encoders in estimating each plane. For f_{CPFDF} , parameters P_1 and P_2 consistently dominate across all cases, while P_3 remains close to zero, suggesting a negligible influence on the estimation. A similar pattern is observed for $f_{\alpha_{\text{INEV}}}$, where P_2 and P_3

TABLE II: Optimized Parameters for 3D Plane Fitting Across Ankle Rotations

Participant	f_{CPFDF}				$f_{\alpha_{\text{INEV}}}$				$f_{\alpha_{\text{IRER}}}$			
	P_1	P_2	P_3	RMSE	P_1	P_2	P_3	RMSE	P_1	P_2	P_3	RMSE
pA	0.295	-0.168	-0.952	2.945 ¹	-0.053	1.009	0.706	1.433 ¹	1.402	-0.047	0.380	1.846 ¹
				2.962 ²				1.453 ²				1.890 ²
pB	0.407	0.033	-0.576	2.147 ¹	-0.040	1.016	0.288	0.980 ¹	1.706	-0.045	0.129	1.674 ¹
				2.188 ²				0.995 ²				1.730 ²
pAB	0.323	-0.123	-0.745	2.536	-0.054	1.009	0.465	1.205	1.522	-0.078	0.282	1.798

Entry pAB represents combined recordings. P_1 , P_2 , and P_3 define the 3D plane orientation, with root-mean-squared error (RMSE) measuring fit accuracy. ¹ and ² denote RMSE values for personalized and generalized models, respectively.

TABLE III: RoM Normalized RMSE values

Partic.	f_{CPDF}		$f_{\alpha_{\text{INEV}}}$		$f_{\alpha_{\text{IRER}}}$	
	nRMSE (%)	RoM (deg)	nRMSE (%)	RoM (deg)	nRMSE (%)	RoM (deg)
pA	4.84 ¹	60.8	4.29 ¹	33.4	3.88 ¹	47.6
	4.86 ²	60.8	4.35 ²	33.4	3.97 ²	47.6
pB	3.39 ¹	63.3	4.83 ¹	20.3	3.52 ¹	37.6
	3.46 ²	63.3	4.91 ²	20.3	3.64 ²	37.6
pAB	3.73	67.9	3.61	33.4	3.78	47.6

Entry pAB represents combined recordings. ¹ and ² denote RMSE values for personalized and generalized models, respectively. nRMSE (%) is normalized as $\text{RMSE}/\text{RoM} \times 100$, using RoM from MOCAP angles and RMSE table III.

emerge as the dominant parameters. In contrast, for $f_{\alpha_{\text{IRER}}}$, parameters P_1 and P_3 are identified as the most influential. In the $f_{\alpha_{\text{INEV}}}$ plane, the parameter P_2 consistently hovers around 1.009 across participants, indicating a strong and stable contribution from a specific orientation in the plane fitting. Furthermore, the RMSE values for $f_{\alpha_{\text{INEV}}}$ are relatively low, suggesting a good overall fit for this motion parameter. For $f_{\alpha_{\text{IRER}}}$, slight variations in P_1 are observed across participants, particularly between the individual models. While the RMSE values for $f_{\alpha_{\text{IRER}}}$ are higher than those for $f_{\alpha_{\text{INEV}}}$, they remain moderate, reflecting a reasonable fit for this parameter.

Overall, participant pB's lower RMSE values across all parameters indicate more consistent and controlled movement patterns in relation to the exoskeleton encoders.

B. Range of Motion Analysis

For additional insights, Fig. 3 illustrates the distribution of measurement points across the RoM for the three ankle

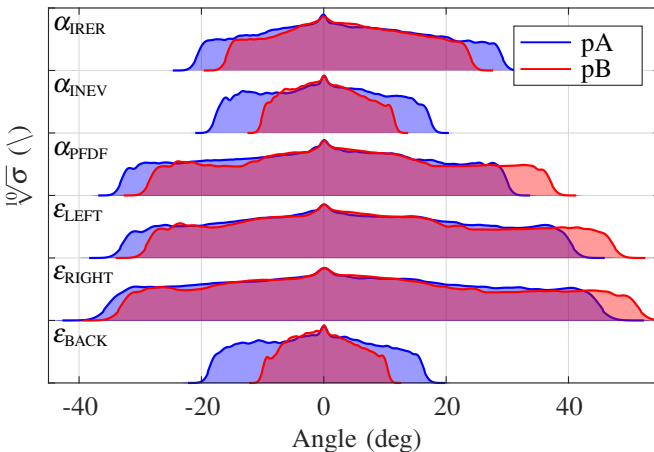


Fig. 3: Visualization of the distribution of ankle joint angles (α_{PDF} , α_{INEV} and α_{IRER}) measured using MOCAP and exoskeleton encoder readings (ϵ_{LEFT} , ϵ_{RIGHT} and ϵ_{BACK}) for two participants. The 10th root scaling of density values improves visualization of data distribution, especially in regions of high density.

angles (α_{PDF} , α_{INEV} and α_{IRER}) alongside the three exoskeleton encoders (ϵ_{BACK} , ϵ_{LEFT} and ϵ_{RIGHT}) for both participants. To improve visualization and address uneven data density, a 10th root scaling is applied to the density values. The intra-participant differences in the RoM for the α_{IRER} and α_{INEV} angles reach up to 10° . Notably, participant pB demonstrates a narrower RoM for both angles.

The RoM of α_{INEV} closely aligns with that of ϵ_{BACK} . Similarly, the RoM of the ϵ_{LEFT} and ϵ_{RIGHT} align with the α_{PDF} for both participants. However, discrepancies are observed between the RoM of the ϵ_{LEFT} , ϵ_{RIGHT} , and α_{PDF} angles.

Given the direct alignment of ϵ_{LEFT} and ϵ_{RIGHT} with the α_{PDF} axis, these differences may indicate either a misalignment between the exoskeleton and the ankle joint or limitations in the MOCAP angle measurement principle described in [7] to fully capture the α_{PDF} movement.

A notable observation in Fig. 3 and Table II is the inter-participant variation in both RoM and RMSE values. Table III addresses this by normalizing the RMSE values to RoM, aiming to reduce the impact of RoM variation. The table presents nRMSE values for the correction factor (f_{CPDF}) and the two ankle angle estimates ($f_{\alpha_{\text{INEV}}}$, and $f_{\alpha_{\text{IRER}}}$) for two participants and two model types (personalized and generalized).

Participant pB demonstrates a smaller RoM for the $f_{\alpha_{\text{INEV}}}$ and $f_{\alpha_{\text{IRER}}}$ estimates compared to participant pA; however, the RoM for f_{CPDF} is of similar magnitude between the two participants. Following normalization of the RMSE, participant pB exhibits lower nRMSE values for both f_{CPDF} and $f_{\alpha_{\text{IRER}}}$. In contrast, the nRMSE value for $f_{\alpha_{\text{INEV}}}$ is higher in participant pB than in participant pA. The data indicate that the nRMSE values for $f_{\alpha_{\text{INEV}}}$ and $f_{\alpha_{\text{IRER}}}$ are much closer when accounting for the differences in RoM. Conversely, the nRMSE values for f_{CPDF} remain distinct even after scaling by RoM, suggesting that the discrepancies in this parameter are more pronounced.

C. Ankle Rotation Estimate

This section examines the ankle joint motion of participant pA, who exhibited higher RMSE values compared to the other participant, necessitating closer analysis. Figure 4 compares MOCAP-derived measurements with encoder-based model predictions for three parameters: α_{PDF} , α_{INEV} , and α_{IRER} . Both participant-specific (pA) and generalized (pAB) models are assessed for normal walking (left column) and stair ascending (right column).

The top row of Figure 4 shows the α_{PDF} parameter, with three estimates compared against the MOCAP data. The first estimate is derived as a simple average of the left and right exoskeleton encoders ($\frac{\epsilon_{\text{LEFT}} + \epsilon_{\text{RIGHT}}}{2}$). The second incorporates a participant-specific correction factor ($f_{\text{CPDF,pA}}$), while the third applies a generalized correction factor ($f_{\text{CPDF,pAB}}$).

For the walking task, correction factors don't visibly improve the $\tilde{\alpha}_{\text{PDF}}$ estimate, though slight improvements are seen during stair ascending. Discrepancies include overestimation of maximum dorsiflexion (DF) during heel touch in walking and pronounced deviation at maximum DF during

stair ascending. However, the model accurately captures minimum values in both tasks.

The $\tilde{\alpha}_{INEV}$ parameter exhibits closer alignment with the MOCAP measurements. Both walking and stair ascending tasks show well-captured trends, but also features small discrepancies. Interestingly, the results indicate no visible differences between the personalized and generalized models, suggesting comparable performance across both conditions.

For $\tilde{\alpha}_{IRER}$, the estimates demonstrate strong agreement with the MOCAP measurements during walking but show a poorer match during stair ascending. Larger deviations occur at extreme angles or during rapid transitions. Similar to $\tilde{\alpha}_{INEV}$, no visible differences are observed between the personalized and generalized models.

IV. DISCUSSION

The proposed approach successfully estimates ankle angles, with better performance for IN/EV and IR/ER compared to PF/DF, where maximum dorsiflexion was not well-captured. A major source of error presumably stems from the misalignment between the exoskeleton's axes and the user's biological joint axes. This misalignment is evidenced by the discrepancies observed between the RoM ankle PF/DF and the corresponding encoder (ϵ_{LEFT} and ϵ_{RIGHT}) readings

from the exoskeleton, as illustrated in Fig. 3. Based on the exoskeleton design, the PF/DF axis of the exoskeleton can be directly aligned with the PF/DF axis of the ankle joint. However, despite efforts to position the exoskeleton in relation to the outer malleolus of the ankle, challenges persist in achieving accurate alignment with the center of rotation of the ankle, particularly given the complexities associated with the 3 DoF design of the exoskeleton. This misalignment impacts the mapping of encoder readings to joint angles, especially for PF/DF, where precise alignment is evidently more critical than for the other two axes (IN/EV and IR/ER). Although users reported a high level of comfort while using the exoskeleton, any compliance in the shoe or attachment mechanism may have further contributed to discrepancies in alignment and motion, potentially affecting the overall effectiveness of the device.

The RMSE values reveal inter-participant variability, with participant pB demonstrating RMSE values nearly 30% lower than those of participant pA, as illustrated in Table II. Notably, RoM between the two participants exhibits visible differences, as depicted in Fig. 3. This variability suggests that individual factors, such as anthropometry and walking style, may play a large role in influencing estimation accuracy. These findings highlight the necessity for improved

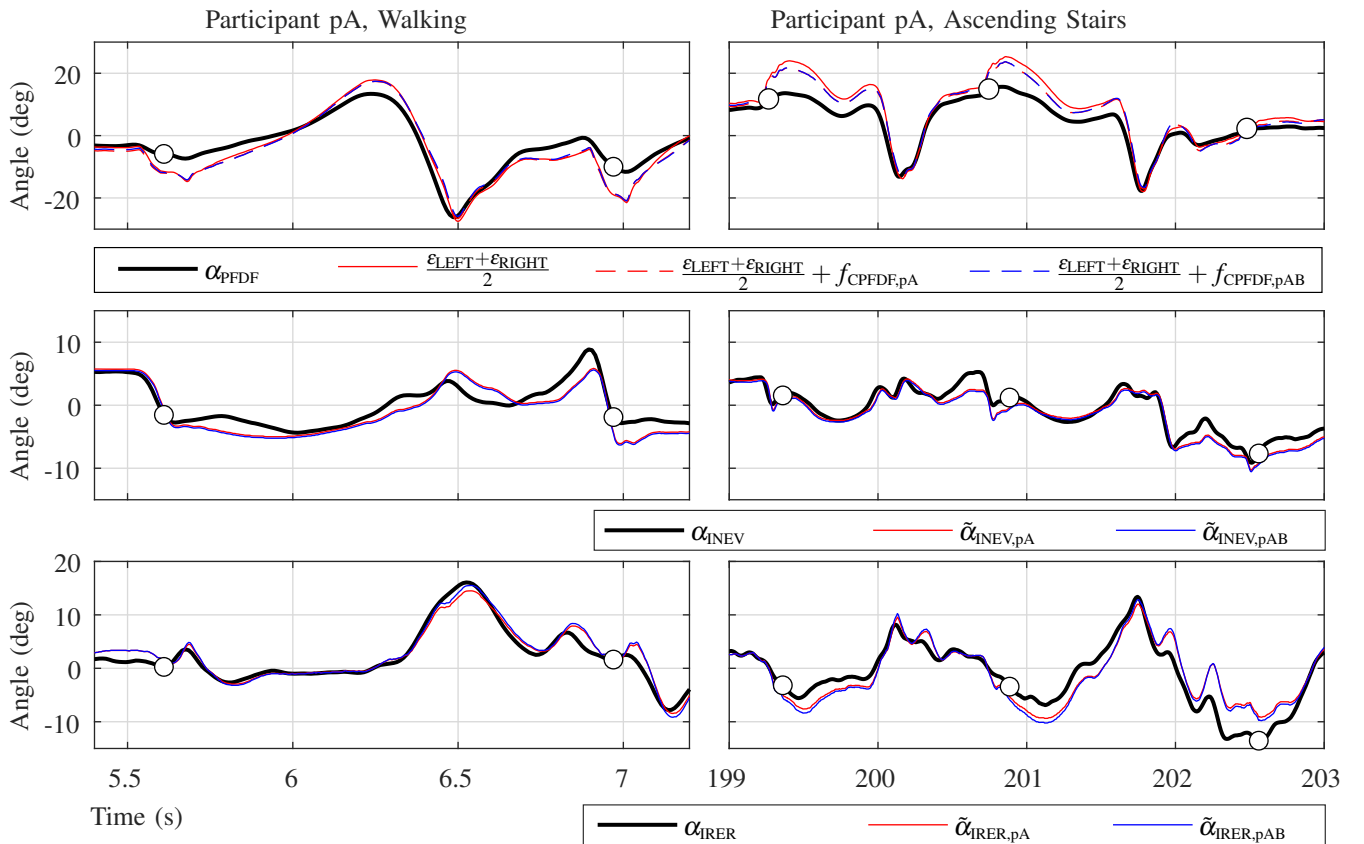


Fig. 4: Comparison of MOCAP-derived measurements (black lines) with encoder-based model predictions for f_{CPDFD} , α_{INEV} , and α_{IRER} . The participant-specific model (pA, red) and generalized model (pAB, blue) are evaluated. The top row shows the effect of correction factors on α_{PDFD} , improving alignment with MOCAP data. The middle and bottom rows illustrate the modeled values of α_{INEV} and α_{IRER} . The white point marks the stride

alignment protocols and the inclusion of larger sample sizes in future studies to enhance the generalizability of model performance. The RMSE values for PF/DF further emphasize the critical importance of achieving proper alignment along this axis to ensure accurate measurements. Consequently, future designs of exoskeletons should prioritize mechanical adjustments aimed at optimizing alignment, particularly for PF/DF, as well as implementing strategies to mitigate the effects of compliance and foot movement within the exoskeleton.

The current methodology, which evaluates each angle separately and relies on plane fitting, may limit the overall accuracy of the model. Personalizing the model yielded only marginal improvements compared to the generalized approach, showing potential for simplifications and generalization. The observed inter-participant variability underscores the necessity of a larger sample size for a robust evaluation of the model. Additionally, observed discrepancies at the peaks of motion indicate that factors such as velocity and dynamic effects, including tissue compliance, need to be integrated into future models. To address these limitations, a more unified approach that combines the assessment of multiple angles and incorporates additional parameters—potentially through machine learning techniques—could enhance both performance and generalizability.

V. CONCLUSION

This study demonstrates the potential of encoder-based models for estimating ankle angles in parallel exoskeletons, but challenges remain due to alignment issues, compliance effects, and inter-participant variability. While the current model is a step toward understanding the relationship between ankle motion and encoder readings, further research is needed to refine the approach. This includes incorporating additional parameters, testing with larger and more diverse participant pools, and exploring more advanced machine learning techniques. Ultimately, these efforts could improve the accuracy and generalizability of the model, paving the way for enhanced exoskeleton performance.

REFERENCES

- [1] K. L. Poggensee and S. H. Collins, "How adaptation, training, and customization contribute to benefits from exoskeleton assistance," *Science Robotics*, vol. 6, no. 58, p. eabf1078, Sep. 2021.
- [2] M. G. Alvarez-Perez, M. A. Garcia-Murillo, and J. J. Cervantes-Sánchez, "Robot-assisted ankle rehabilitation: A review," *Disability and Rehabilitation: Assistive Technology*, vol. 15, no. 4, pp. 394–408, May 2020.
- [3] J. L. McGinley, R. Baker, R. Wolfe, and M. E. Morris, "The reliability of three-dimensional kinematic gait measurements: A systematic review," *Gait & Posture*, vol. 29, no. 3, pp. 360–369, 2009.
- [4] G. Zhang, S. Cao, C. Wang, X. Ma, X. Wang, J. Huang, and C. Zhang, "Effect of a Semirigid Ankle Brace on the In Vivo Kinematics of Patients with Functional Ankle Instability during the Stance Phase of Walking," *BioMed Research International*, vol. 2019, pp. 1–10, 2019.
- [5] J. Bessler-Etten, L. Schaake, G. B. Prange-Lasonder, and J. H. Burke, "Assessing effects of exoskeleton misalignment on knee joint load during swing using an instrumented leg simulator," *Journal of NeuroEngineering and Rehabilitation*, vol. 19, no. 1, p. 13, 2022. [Online]. Available: <https://jneuroengrehab.biomedcentral.com/articles/10.1186/s12984-022-00990-z>

- [6] T. Moeller, F. Moehler, J. Krell-Roesch, M. Dežman, C. Marquardt, T. Asfour, T. Stein, and A. Woll, "Use of lower limb exoskeletons as an assessment tool for human motor performance: A systematic review," *Sensors*, vol. 23, no. 6, 2023.
- [7] M. Dežman, C. Marquardt, and T. Asfour, "Ankle exoskeleton with a symmetric 3 dof structure for plantarflexion assistance," in *IEEE International Conference on Robotics and Automation (ICRA)*, Yokohama, Japan, May 2024.
- [8] K. A. Witte and S. H. Collins, "Design of Lower-Limb Exoskeletons and Emulator Systems," in *Wearable Robotics*, J. Rosen and P. W. Ferguson, Eds. Elsevier, 2020, pp. 251–274.
- [9] A. Weerasingha, A. Pragnathilaka, W. Withanage, R. Ranaweera, and R. Gopura, "C-JAE: 3 DOF Robotic Ankle Exoskeleton with Compatible Joint Axes," in *2018 Moratuwa Engineering Research Conference (MERCCon)*. Moratuwa: IEEE, May 2018, pp. 270–275.
- [10] M. B. Hong, G. T. Kim, and Y. H. Yoon, "ACE-Ankle: A Novel Sensorized RCM (Remote-Center-of-Motion) Ankle Mechanism for Military Purpose Exoskeleton," *Robotica*, vol. 37, no. 12, pp. 2209–2228, 2019.
- [11] L. M. Mooney and H. M. Herr, "Biomechanical walking mechanisms underlying the metabolic reduction caused by an autonomous exoskeleton," *Journal of NeuroEngineering and Rehabilitation*, vol. 13, no. 1, p. 4, Dec. 2016.
- [12] Z. Que and K.-M. Lee, "Magnetic Pantographic Exoskeleton Illustrated With a Biomimetic Ankle-Foot Simulator for 3-DOF Noncontact Actuation/Measurements," *IEEE/ASME Transactions on Mechatronics*, vol. 29, no. 4, pp. 3028–3037, 2024. [Online]. Available: <https://ieeexplore.ieee.org/document/10549930/>
- [13] S. Lee, J. Kim, L. Baker, A. Long, N. Karavas, N. Menard, I. Galiana, and C. J. Walsh, "Autonomous multi-joint soft exosuit with augmentation-power-based control parameter tuning reduces energy cost of loaded walking," *Journal of NeuroEngineering and Rehabilitation*, vol. 15, no. 1, p. 66, Dec. 2018.
- [14] L. N. Awad, J. Bae, K. O'Donnell, S. M. M. De Rossi, K. Hendron, L. H. Sloop, P. Kudzia, S. Allen, K. G. Holt, T. D. Ellis, and C. J. Walsh, "A soft robotic exosuit improves walking in patients after stroke," *Science Translational Medicine*, vol. 9, no. 400, p. eaai9084, Jul. 2017.
- [15] B. He, M. Li, R. Liang, Z. Liang, W. Yao, S. Sareh, J. Xie, G. Xu, and Y. Noh, "Optoelectronic-Based Pose Sensing for a Hand Rehabilitation Exoskeleton Continuous Structure," *IEEE Sensors Journal*, vol. 22, no. 6, pp. 5606–5615, 2022.
- [16] Y. Mengüç, Y.-L. Park, H. Pei, D. Vogt, P. M. Aubin, E. Winchell, L. Fluke, L. Stirling, R. J. Wood, and C. J. Walsh, "Wearable soft sensing suit for human gait measurement," *The International Journal of Robotics Research*, vol. 33, no. 14, pp. 1748–1764, 2014.
- [17] D. Goto, Y. Sakaue, T. Kobayashi, K. Kawamura, S. Okada, and N. Shiozawa, "Bending Angle Sensor Based on Double-Layer Capacitance Suitable for Human Joint," *IEEE Open Journal of Engineering in Medicine and Biology*, vol. 4, pp. 129–140, 2023.
- [18] R. M. Chapman, M. T. Torchia, J.-E. Bell, and D. W. Van Citters, "Assessing Shoulder Biomechanics of Healthy Elderly Individuals During Activities of Daily Living Using Inertial Measurement Units: High Maximum Elevation Is Achievable but Rarely Used," *Journal of Biomechanical Engineering*, vol. 141, no. 4, p. 041001, 2019.
- [19] B. H. Kim, S. H. Hong, I. W. Oh, Y. W. Lee, I. H. Kee, and S. Y. Lee, "Measurement of Ankle Joint Movements Using IMUs during Running," *Sensors*, vol. 21, no. 12, p. 4240, 2021.
- [20] J. C. Arceo, L. Yu, and S. Bai, "Robust Sensor Fusion and Biomimetic Control of a Lower-Limb Exoskeleton With Multimodal Sensors," *IEEE Transactions on Automation Science and Engineering*, pp. 1–11, 2024.
- [21] R. Kianifar, V. Joukov, A. Lee, S. Raina, and D. Kulić, "Inertial measurement unit-based pose estimation: Analyzing and reducing sensitivity to sensor placement and body measures," *Journal of Rehabilitation and Assistive Technologies Engineering*, vol. 6, p. 2055668318813455, 2019. [Online]. Available: <https://journals.sagepub.com/doi/10.1177/2055668318813455>
- [22] K. Zhu, J. Li, D. Li, B. Fan, and P. B. Shull, "IMU Shoulder Angle Estimation: Effects of Sensor-to-Segment Misalignment and Sensor Orientation Error," *IEEE Transactions on Neural Systems and Rehabilitation Engineering*, vol. 31, pp. 4481–4491, 2023. [Online]. Available: <https://ieeexplore.ieee.org/document/10312740/>